In-fiber fluorospectroscopy based on a spectral decomposition method

Yong, Derrick; Lee, Elizabeth; Yu, Xia; Chan, Chi Chiu

2014

Yong, D., Lee, E., Yu, X., & Chan, C. C. (2014). In-fiber fluorospectroscopy based on a spectral decomposition method. Optics Express, 22(19), 23640-.

https://hdl.handle.net/10356/81404

https://doi.org/10.1364/OE.22.023640

In-fiber fluorospectroscopy based on a spectral decomposition method

Derrick Yong,[1,2] Elizabeth Lee,[1,2] Xia Yu, [1,*] and Chi Chiu Chan[2,^]

[1]*Precision Measurements Group, Singapore Institute of Manufacturing Technology, 71 Nanyang Drive, Singapore 638075*

[2]*Division of Bioengineering, School of Chemical and Biomedical Engineering, Nanyang Technological University, 70 Nanyang Drive, Singapore 637457*

[*]*xyu@SIMTech.a-star.edu.sg* *[^]ecchan@NTU.edu.sg*

Abstract: We report a simplified model for the computation of light-fluorescence interactions within photonic crystal fibers (PCFs). It involved the plotting of ray trajectories confined by total internal reflection within a geometrically simplified PCF core. This was followed by the calculation of absorption and fluorescence emission at each point of reflection, which were subsequently summed and averaged over all the launched rays. The computation of these components for two specified wavelengths (peak excitation and emission) produced a dimensionless ratiometric relationship for varying concentrations of fluorescence dye. This hence eliminated the need for optical filters and minimized the effects of intensity fluctuations. Modeled results were demonstrated to concur well with that obtained experimentally for two PCFs with different microstructured cores.

OCIS codes: (060.5295) Photonic crystal fibers; (060.2370) Fiber optics sensors; (080.0080) Geometric optics; (300.6280) Spectroscopy, fluorescence and luminescence.

References and links

1. P. Russell, "Photonic crystal fibers," Science **299**, 358-362 (2003).
2. J. C. Knight, "Photonic crystal fibres," Nature **424**, 847-851 (2003).
3. O. Frazão, J. L. Santos, F. M. Araújo, and L. A. Ferreira, "Optical sensing with photonic crystal fibers," Laser Photonics Rev **2**, 449-459 (2008).
4. A. S. J. Cerqueira, "Recent progress and novel applications of photonic crystal fibers," Rep Prog Phys **73**, 024401 (2010).
5. A. M. R. Pinto, and M. Lopez-Amo, "Photonic Crystal Fibers for Sensing Applications," Journal of Sensors **2012**, 21 (2012).
6. A. M. Cubillas, S. Unterkofler, T. G. Euser, B. J. M. Etzold, A. C. Jones, P. J. Sadler, P. Wasserscheid, and P. S. J. Russell, "Photonic crystal fibres for chemical sensing and photochemistry," Chem Soc Rev (2013).
7. J. C. Knight, T. A. Birks, P. S. J. Russell, and D. M. Atkin, "All-silica single-mode optical fiber with photonic crystal cladding," Opt Lett **21**, 1547-1549 (1996).
8. M. M. Tanya, B. Walter, F. Kentaro, C. B. Joanne, N. G. R. Broderick, and D. J. Richardson, "Sensing with microstructured optical fibres," Meas Sci Technol **12**, 854 (2001).
9. X. Yu, Y. C. Kwok, N. A. Khairudin, and P. Shum, "Absorption detection of cobalt(II) ions in an index-guiding microstructured optical fiber," Sensors and Actuators B: Chemical **137**, 462-466 (2009).
10. X. Yu, Y. Sun, G. B. Ren, P. Shum, N. Q. Ngo, and Y. C. Kwok, "Evanescent Field Absorption Sensor Using a Pure-Silica Defected-Core Photonic Crystal Fiber," Photonics Technology Letters, IEEE **20**, 336-338 (2008).
11. X. Yu, Y. Zhang, Y. C. Kwok, and P. Shum, "Highly sensitive photonic crystal fiber based absorption spectroscopy," Sensor Actuat B-Chem **145**, 110-113 (2010).
12. G. Pickrell, W. Peng, and A. Wang, "Random-hole optical fiber evanescent-wave gas sensing," Opt Lett **29**, 1476-1478 (2004).
13. Y. L. Hoo, W. Jin, C. Shi, H. L. Ho, D. N. Wang, and S. C. Ruan, "Design and Modeling of a Photonic Crystal Fiber Gas Sensor," Appl Opt **42**, 3509-3515 (2003).
14. S. Afshar V, S. C. Warren-Smith, and T. M. Monro, "Enhancement of fluorescence-based sensing using microstructured optical fibres," Opt Express **15**, 17891-17901 (2007).

15. O. S. W. Gareth, G. E. Tijmen, J. R. Philip St, and C. J. Anita, "Spectrofluorimetry with attomole sensitivity in photonic crystal fibres," Method Appl Fluoresc **1**, 015003 (2013).
16. M. Dandin, P. Abshire, and E. Smela, "Optical filtering technologies for integrated fluorescence sensors," Lab Chip **7**, 955-977 (2007).
17. Y. Maruyama, K. Sawada, H. Takao, and M. Ishida, "A novel filterless fluorescence detection sensor for DNA analysis," IEEE Trans Electron Devices **53**, 553-558 (2006).
18. H. Nakazawa, M. Ishida, and K. Sawada, "Multimodal bio-image sensor for real-time proton and fluorescence imaging," Sensor Actuat B-Chem **180**, 14-20 (2013).
19. K. Yamasaki, H. Nakazawa, N. Misawa, M. Ishida, and K. Sawada, "Multicolor fluorescence detection for single nucleotide polymorphism genotyping using a filter-less fluorescence detector," Appl Phys Lett **102**, - (2013).
20. N. Hirokazu, Y. Keita, T. Takuya, A. Ippei, I. Makoto, and S. Kazuaki, "Improvement of the Detection Accuracy and Detection Limit of a Filter-less Fluorescence Detector," Appl Phys Express **6**, 077001 (2013).
21. S. Chen, A. Rajagopal, and A. Scherer, "Filterless time-domain detection of one or more fluorophores," (Google Patents, 2013).
22. H. Wang, Y. Qi, T. J. Mountziaris, and C. D. Salthouse, "A portable time-domain LED fluorimeter for nanosecond fluorescence lifetime measurements," Rev Sci Instrum **85**, - (2014).
23. C. D. Salthouse, R. Weissleder, and U. Mahmood, "Development of a time domain fluorimeter for fluorescent lifetime multiplexing analysis," IEEE Trans Biomed Circuits Syst **2**, 204-211 (2008).
24. A. Demchenko, "The Concept of λ-Ratiometry in Fluorescence Sensing and Imaging," J Fluoresc **20**, 1099-1128 (2010).
25. D. Yong, W. L. Ng, X. Yu, and C. C. Chan, "A compact opto-fluidic platform for chemical sensing with photonic crystal fibers," Sensor Actuat A-Phys **191**, 22-26 (2013).
26. Y. Yuan, and L. Ding, "Theoretical investigation for excitation light and fluorescence signal of fiber optical sensor using tapered fiber tip," Opt Express **19**, 21515-21523 (2011).
27. R. M. Chyad, M. Z. M. Jafri, K. N. Mutter, and K. Ibrahim, "Numerical ray tracing through a modified cladding fiber optic segment sensors," Optik **123**, 860-862 (2012).
28. X. Yu, P. Shum, G. B. Ren, and N. Q. Ngo, "Photonic crystal fibers with high index infiltrations for refractive index sensing," Opt Commun **281**, 4555-4559 (2008).
29. W. F. Love, L. J. Button, and R. E. Slovacek, "Optical Characteristics of Fiberoptic Evanescent Wave Sensors," in *Biosensors with Fiberoptics*, D. Wise, and L. Wingard, Jr., eds. (Humana Press, 1991), pp. 139-180.
30. M. Heiblum, and J. Harris, "Analysis of curved optical waveguides by conformal transformation," IEEE J Quantum Electron **11**, 75-83 (1975).
31. R. T. Schermer, and J. H. Cole, "Improved Bend Loss Formula Verified for Optical Fiber by Simulation and Experiment," IEEE J Quantum Electron **43**, 899-909 (2007).
32. M. Milosevic, "Anatomy of ATR Absorption," in *Internal Reflection and ATR Spectroscopy*(John Wiley & Sons, Inc., 2012), pp. 67-78.
33. R. Sjöback, J. Nygren, and M. Kubista, "Absorption and fluorescence properties of fluorescein," Spectrochim Acta Mol Biomol Spectros **51**, L7-L21 (1995).
34. S. Bidmanova, A. Hlavacek, J. Damborsky, and Z. Prokop, "Conjugation of 5(6)-carboxyfluorescein and 5(6)-carboxynaphthofluorescein with bovine serum albumin and their immobilization for optical pH sensing," Sensor Actuat B-Chem **161**, 93-99 (2012).
35. N. A. Mortensen, J. R. Folken, P. M. W. Skovgaard, and J. Broeng, "Numerical aperture of single-mode photonic crystal fibers," IEEE Photon Technol Lett **14**, 1094-1096 (2002).

1. Introduction

The devise of photonic crystal fibers (PCFs) [1, 2] has opened a myriad of new avenues in the field of fiber optic technology. In particular, their periodic arrays of laterally-running microstructured air holes serve not only to confine and guide light via novel means, but further as fillable channels for in-fiber light-matter interactions – seeing to their numerous applications [3-6]. Index guiding PCFs, a class of PCF that guides light via modified total internal reflection (TIR) [7], offer broadband guidance and surface-specific light-matter interactions. The latter being manipulable by microstructure variations [8], has allowed for their applications in absorption spectroscopy of liquids [9-11] and gases [12, 13], as well as fluorescence spectroscopy [14, 15].

Often in the above employment of PCFs, the interfacing of optical fiber components to conventional optics involves bulky and component-intensive set-ups that largely overshadow

the compactness and flexibility offered by fiber optics. In fluorospectroscopy, specifically, there is the further requirement of optical filters and/or laser sources. These serve to remove or allow for easy disregard of the remaining excitation, but are however extremely space consuming and often costly. Although several fluorospectroscopy approaches circumvent the need for traditional or physical optical filters, they involve using complex micro architectures that filter [16] or are spectrally selective detectors [16-20]; require highly precise detectors for fluorescent lifetime measurements [21-23]; or entail the use of an additional reference emitter for ratiometry [24].

Hence, to maintain the simplicity and low-cost of our previously reported all-fiber opto-fluidic platform [25], a mathematical spectral decomposition approach was employed. In brief, it characterizes the ratiometric change between the collected intensities at two specified wavelengths upon fluorescence dye concentration variations. This contrasts their respective remaining excitation and produced fluorescence emission, and provides a dimensionless relationship that mitigates the undesirable effects of intensity fluctuations. Since the region of light confinement and propagation in PCFs, namely its core, possesses dimensions relatively larger than the employed wavelength [26, 27], a ray-tracing approach was deemed a suitable approximation to model the in-fiber light-matter interactions. This is in general a less computationally intensive approach as compared to mode solutions computed from Maxwell's equations employed in fundamentally similar index guiding microstructured optical fibers, used in fluorospectroscopy [14]. On the other hand, the model also complements the cuvette-like fluorospectroscopic methods performed in photonic bandgap guiding PCFs [15].

This paper focuses on the development of a ray-tracing model capable of accounting for the constituents – remaining excitation and produced emission – of the dimensionless ratiometric change over various dye concentrations. This was subsequently employed in the calculations for two PCFs, namely a defected-core PCF (dcPCF) [10] and a solid-core PCF (scPCF) [28]. These were then compared with experimentally obtained results for the corresponding PCFs loaded with varying concentrations of a common fluorescence dye – carboxyfluorescein.

2. Materials and Methods

2.1 Chemicals and Other Materials

5(6)-Carboxyfluorescein (CF) was purchased from Sigma-Aldrich (Singapore). 1M Tris buffer at pH8.8 was obtained from 1st Base (Singapore). All other chemicals were of reagent grade.

2.2 Optofluidic platform set-up

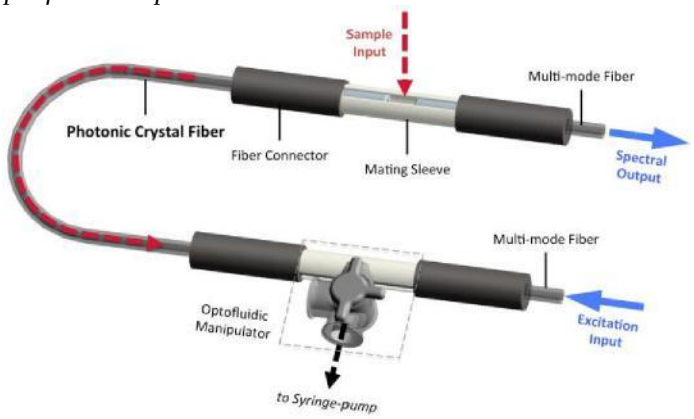

Fig. 1. 3D schematics of optofluidic platform.

The set-up, as shown in Fig. 1, comprises: (1) a blue (490nm) fiber-coupled LED (Thorlabs M490F1) as the excitation input; (2) a spectrometer (Ocean Maya 2000) for the spectral output collection; (3) a series of optical fibers (input & output multi-mode fibers and a length of PCF as the sensing element), fiber connectors and adapters; (4) a syringe-pump-attached opto-fluidic manipulator described earlier in [25]. The 105mm length of PCF is bent into a U-shape with a semi-circle segment, of bending radius $_{(Rbend)}$ 12.5mm, flanked by two equal straight segments.

A series of CF solutions, dissolved to various concentrations (10-100µM) in 321mM Tris buffer, was infiltrated into the bent of length PCF with their resultant output spectra collected subsequently. The ratio between the intensities at λ_{exc}=490nm and λ_{ems}=510nm ($I(\lambda_{ems})/I(\lambda_{exc})$) was then recorded per concentration.

2.3 Ray-tracing model

To support the proposed spectral interpretation, a ray-tracing model describing fluorescence excitation and collection at the exposed surface of a conventional optical fiber [29] was adapted. Each ray, defined by its initial spatial location and angle of launch, has its trajectory and incident angles traced via simple geometrical constraints. Using the light-fluorescence interactions at each point of incidence and its number of occurrences, the spectral variations per concentration of CF, $_{I(\lambda ems)/I(\lambda exc)}$ in particular, can thus be derived.

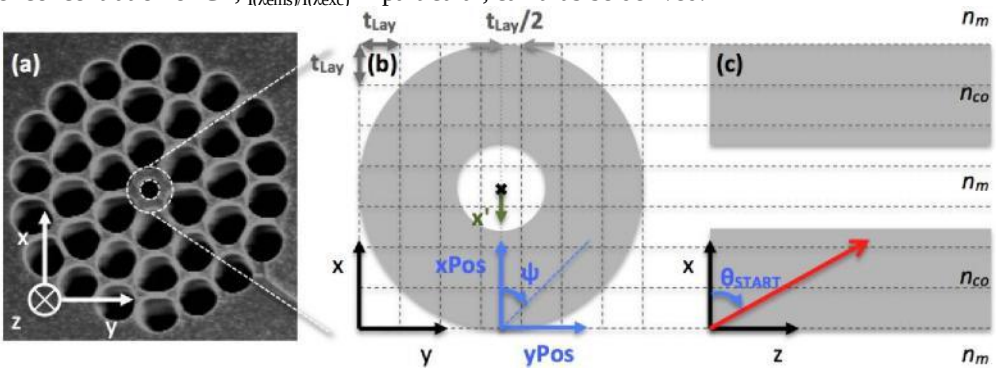

Fig. 2. (a) Micrograph of dcPCF's microstructure with its core highlighted by white circles. Corresponding (b) transverse and (c) longitudinal cross-section of dcPCF's core, defining the coordinate system (in black and green) and launch parameters (in blue). The launched ray (in red) indicated has an initial spatial location of xPos=yPos=0, tilt of 0˚ and launch angle of θ_{START}.

The launch condition per ray was determined by a combination of parameters (illustrated in Fig. 2b and c), namely its (1) x- and y-position of launch (xPos and yPos respectively); (2) angle of launch $_{(\theta START),}$ on its plane of launch; (3) tilt (ψ) of its plane of launch. This is with the assumption that the core of the dcPCF, of diameter $_{Dcore,}$ can be approximated as a cylinder with a hollowed-core, of diameter $_{Ddef\text{-}core.}$ The aforementioned core is defined as the central region surrounded by the innermost ring of air holes as indicated in Fig. 2a. The same approximation was made for the scPCF, however, with its $_{Ddef\text{-}core}$ ignored.

In order to incorporate the effect of bending, a graded core refractive index (n_j profile was adopted. Bending is assumed here to have negligible effect on the medium refractive index (n_m), which is fluid in nature. The bending-induced refractive index change was governed by the following equation [30, 31]:

(1)

Where positive x' (as indicated in Fig. 2b) was towards the exterior of the bend with a bending radius, $_{Rbend.}$ It should be noted that bending only alters $_{nco}$ along the x-axis, $_{nco}$ is

hence a constant in the y- and z- direction. Here, the layer thickness (t_{Lay}) – equivalent to D_{core}

Now, transforming the earlier discussed ray-trace into a 3D format (when $\psi \neq 0$), where each layer is converted into a cuboid element as illustrated in Fig. 4 (detailed derivations as

divided by the total number of layers (Lay_{Tot}) – served to provide a discretization to the $n_{co,bent}$ distribution as well as defined the mesh density of the x-y grid. This meant a density equivalent to $_{LayTot2,}$ where each x-y coordinated corresponded to a point of launch as indicated by the intersecting dotted lines in Fig. 2b. Subsequently, from each launched ray, a set of geometrically derived values was obtained: (1) number of reflections (N_{Refl}); (2) $n_{co,bent}$ at point of incidence; (3) incident angle (a).

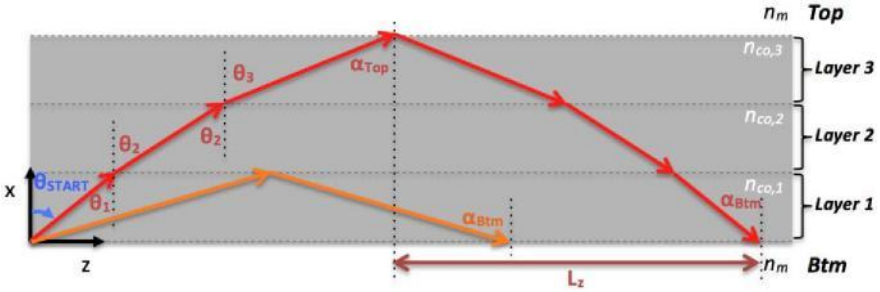

Fig. 3. Path of ray (in red) through 3 discretized layers with differing $_{nco,}$ resulting in an incident angle at Layer 3-Top interface (a_{Top}) and one at the Layer 1-Btm interface (a_{Btm}), as well as a longitudinal displacement of L_z between the two incidences. Path of an intra-core reflected ray (in orange) is similarly indicated. (Note: Exterior of bend is towards the bottom, i.e. $n_{co,1}>n_{co,2}>n_{co,3}$ and $\theta_1<\theta_2<\theta_3$.)

A launched ray traverses the discretized layers undergoing refraction each time it crosses a layer-layer interface, bending away from the normal as it propagates in the positive x-direction – where $_{nco,bent}$ decreases. Refraction continues until the ray experiences TIR, particularly when it meets the medium of a significantly lower n, or in unique scenarios between $n_{co,bent}$ layers, when $_{\theta START}$ tends towards 90˚, as depicted by the orange coloured ray in Fig. 3. Based on this, a is obtained for reflections off the top and bottom interfaces, $_{aTop}$ and a_{Btm} respectively, or just a_{Btm} for the latter mentioned intra-core reflection. Concomitantly, n_{co} of the layer where reflections occurred were recorded. Next, using the longitudinal distance between TIR events, defined as L_z in Fig. 3, $_{NRefl}$ can be calculated from the total length of PCF (L_{PCF}) under study.

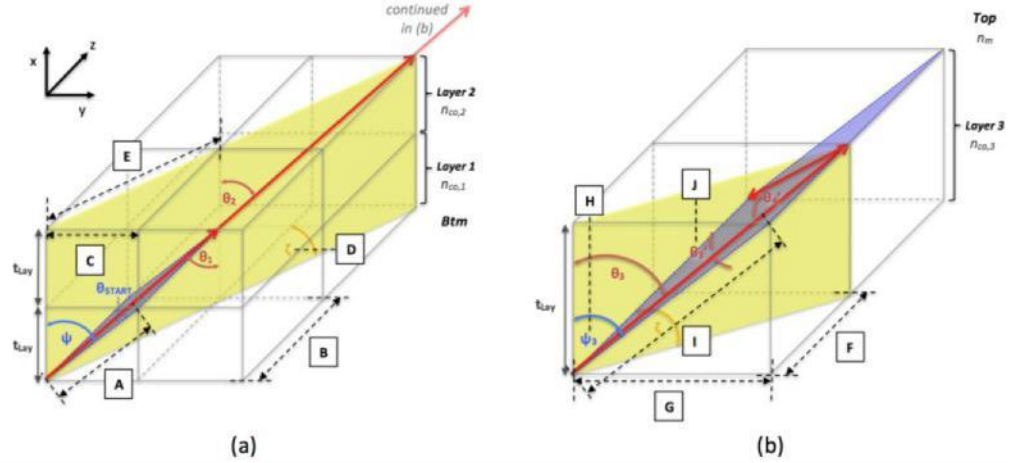

Fig. 4. Path of ray (in red) undergoing (a) refraction and (b) reflection in a 3D-domain, launched at a tilt of ψ. Plane of launch (for (a)) or incidence (for (b)) and Plane of refraction is highlighted in blue and yellow, correspondingly.

well as rotated perspectives can be found in the Appendix). Drawing further geometrical relationships and employing Snell's Law, the following is derived for the refraction regime shown in Fig. 4a:

(2)

Consequently, the longitudinal displacement of the refracted ray is:

(3)

Similarly, the same was performed for the reflection regime, shown in Fig. 4b, and the incident angle is given as:

(4)

Reflection in the plane of incidence, at the Top core-medium interface, gives an incident angle $_{aTop=02'}$, which is also equivalent to the reflected angle θ_3'. It should also be highlighted here that reflection is assumed to occur along the edge of the cuboid, which defines the plane of incidence. Likewise, the above can be rewritten to accommodate rays launched at $\psi>90^{\circ}$.

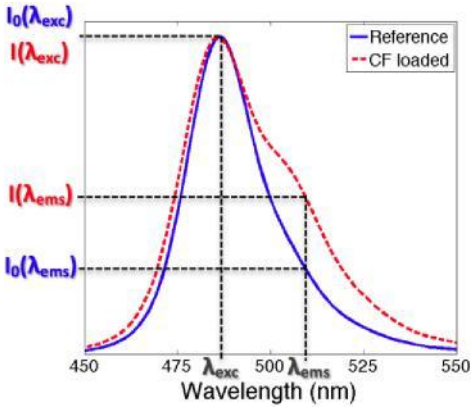

Fig. 5. Output spectrum of buffer (solid blue line) and 30μM CF (red dotted line) loaded dcPCF normalized to $_{I0(\lambda exc)}$ and $_{I(\lambda exc)}$ respectively.

Generally, the emission of fluorescence presents as a shoulder on the right flank of the remaining excitation source, as depicted by the red-dotted spectrum in Fig. 5. This stems from the fact that the spectrum of fluorescence emission overlaps that of the remaining excitation, essentially implying that $I(\lambda)$ is a superposition of the two. Employing that derived above with the assumption of negligible dispersion between the wavelengths in the studied span, the specific extent of this light-fluorescence interaction could then be calculated. These could subsequently be fitted into the following equation describing $_{I(\lambda ems)/I(\lambda exc)}$, where λ_{exc}=490nm and λ_{ems}=510nm correspond to the peak absorption and emission wavelengths respectively. Its dimensionless form eliminates the common but undesirable effects of intensity fluctuations – typical of optical set-ups.

(5)

Considering the earlier mentioned spectral superposition, $I(\lambda)$ was decomposed into its $_{IFlnorm}(I_{exc}) + (1 - f_{abexc})$ various constituents – I_{FI}: Intensity of fluorescence emission; I_0: Initial (or reference) intensity; I_{abs}: Intensity absorbed – with the assumption of negligible reabsorption at low CF

Now, transforming the earlier discussed ray-trace into a 3D format (when $\psi\neq0$), where each layer is converted into a cuboid element as illustrated in Fig. 4 (detailed derivations as

concentrations. $_{(I0-Iabs)}$ being a representation of the remaining excitation. In addition, to simplify subsequent calculations, its components were normalized to $_{I0(\lambda exc)}$ and a fraction of absorption $_{(fabs),}$ relative to $I_0(\lambda)$, was introduced.

The above would be calculated for each launched ray and averaged, which effectively involved a 4D matrix (xPos by $_{\theta START}$ by yPos by ψ) representing all the ray launch conditions. Consequently, $_{IFl,norm}$ and $_{fabs}$ were calculated by adapting the method described in [29], and are detailed as follows.

$I_{Fl,norm}$ comprises the total fluorescence emission generated per launched ray. This would be the sum of emission resulting from all reflections off the core-medium interfaces, where each of these emissions is given by:

(6)

It is noteworthy to highlight here that the above describes the emission resulting from the excitation at λ by a normalized excitation intensity of $_{I0(\lambda)/I0(\lambda exc).}$ c, ε and $_{\Phi Fl}$ represent the concentration, extinction coefficient and quantum yield of the fluorescence dye, correspondingly. $_{fFl,\lambda}$ is the fraction of emission at $_{\lambda ems}$ or $_{\lambda exc.}$ Lastly, $_{Fabs}$ and $_{Pemit}$ is the factor of absorption and the probability of emission collection respectively. These two terms are integrated over δ, which is the perpendicular distance from the core-medium interface extended infinitely into the medium.

The factor of absorption, $_{Fabs,}$ is defined by:

(7)

Where $_{Pabs}$ is the power absorbed per unit volume and $_{nrel}$ is the relative refractive index ($n_{co,bent}/n_m$), while the penetration depth, d_p, is:

(8)

It should be highlighted that in all calculations of $_{nrel,}$ n_m is assumed to be a constant equivalent to that of water, due to the negligible influence that low concentrations of solutes (fluorescence dye in this case) has on refractive index.

On the other hand, the probability of emission collection, $_{Pemit,}$ which discriminates for forward propagating (positive z-direction) rays:

(9)

P_1Where $dP_{\#}/d\Omega$ is the dipole radiation near a dielectric interface (the core-medium interface in

$$\int_0^{\frac{\pi}{2}} \frac{dP}{d\Omega} \sin\alpha\, d\alpha + \int_{\frac{\pi}{2}}^{\pi} \frac{dP_3}{d\Omega} \sin\alpha\, d\alpha$$

this case) per unit solid angle ($d\Omega$), averaged over all dipole orientations. The subscript "#" corresponds to the different ranges of α between 0 and π, and are described in the Appendix.

From $_{Fabs,}$ the fraction of absorption, $_{fabs,}$ was derived as [32]:

(10)

As mentioned earlier, each launched ray experiences top and/or bottom reflections off the core-medium interface. This therefore leads to a distinct value for each interfacial reflection –

$S_{ray,Top}$ and $S_{ray,stm}$ as well as $f_{dbs,Top}$ and $f_{abs,Btm}$, corresponding to their respective a and n_{co} values.

Further to which, as a fraction of I_0 is absorbed after each reflection, $_{IFl,norm}$ is not a mere multiplication of S_{ray} by its total number of occurrence $_{(NRefl).}$ Instead, it is expressed in the following two summations derived from the geometric progression of successive absorptions, one for top-and-bottom reflections $_{(\Sigma Sray,TopBtm)}$ and the other for intra-core reflections, where the latter involves bottom-only reflections ($\Sigma S_{ray,BtmONLY}$).

(11)

$$S$$ (12)

Summing the above two equations $_{f}$or all λ gives the $I_{Fl,norm}$ for each launched ray gives: $_{Fl}$

(13)

Similarly, the following two equations account for the fraction of remaining input intensity after absorption (1-f_{abs}) for λ_{ems} and λ_{exc}.

(14)

(15)

In the light of the above Eqs. (6)-(15), only those rays capable of propagating through the core, in order to fulfil the requirements of TIR, were considered, the rest were omitted. The remaining input excitation. This reduced $_{I(\lambda ems)/I(\lambda exc)}$ to a ratio between the emission at λ_{ems} and λ_{exc} as shown below.

(16)

The above discussed ray-tracing model was translated into an algorithm in MATLAB and employed in the calculations for the following definitions and launch parameters, which were selected to closely match experimental conditions – D_{in}=10 μm and D_{out}=4 μm; R_{out}=125 mm and $L_{cr}=R_{out}\pi$; n_{clad}=1.462 and n_{in}=1.373 (based on λ_{exc}=490 nm); hence $\theta_{Crit}=\sin^{-1}(n_{in}/n_{clad})$=66.1°; λ_{exc}=400-600 nm; t_{Lay}=10 and $t_{Lay}=D_{in}$; yPos=0 to D_{in} at intervals of t_{Lay}; yPos=0 and $t_{Lay}/2$ to ($D_{core}/2$-t_{Lay}) at intervals of t_{Lay}; $\theta_{START}=\theta_{Crit}$ to (θ_{Crit}+0.9°) at intervals of 0.1°, (θ_{Crit}+1°) to 88° at intervals of 1° and 88° to 89.9° at intervals of 0.1°; ψ=0 to 170° at intervals of 10°. It should be noted that yPos and ψ were only calculated for half the core diameter and the ray-tracing algorithm was set to equally weight according to the respective launch angle. For comparison, 100 μM of Methyl Green was prepared in ethanol and experimentally, θ_{Crit}=63.3° [33,34], f_{abs}=0.75 at λ_{exc}=405 nm (from Life Technologies' online database). This was likewise done for a PCF with D_{in}=1.8 μm and D_{out}=0.4 μm.

Results and Discussion

The calculated $_{I(\lambda ems)/I(\lambda exc)}$ values from the ray-trace model were contrasted with those obtained experimentally. This was similarly done for an unbent or straight length of PCF (i.e. $R_{bend}=\infty$). However, based on the numerical aperture calculation described in [35], the θ_{START}

range for the straight dcPCF was shortened to $\theta_{START}= (\theta_{Crit}+19)$ to 88 at intervals of 1 and 88 to 89.9 at intervals of 0.1, which more closely concurs with single-mode operation. On the other hand, $\theta_{START}=(\theta_{Crit}+21)$ to 88 at intervals of 1 and 88 to 89.9 at intervals of 0.1 for the straight scPCF.

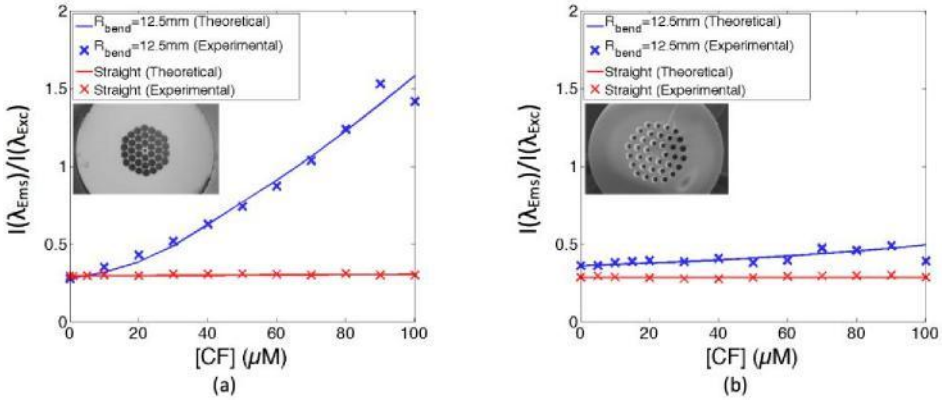

Fig. 6. Comparison of $I_{(\lambda ems)/I(\lambda exc)}$ for (a) dcPCF and (a) scPCF. Solid lines represent that calculated from the theoretical ray-trace model, while crosses are for that obtained experimentally for bent (in blue) and straight (in red) PCFs. Insets: Corresponding micrographs of the PCFs' transverse cross-sections.

The comparison in Fig. 6a showed good agreement between the theoretical and experimental results for the dcPCF. Contrasting the results between its bent and straight configurations, indicated the θ_{START} span as the primary reason for their distinction. Where smaller θ_{START} values (present only in the bent dcPCF calculations) resulted in smaller a, leading to larger S_{rav} and f_{abs} values, as described by Eq. **(6)** and **(10)** respectively.

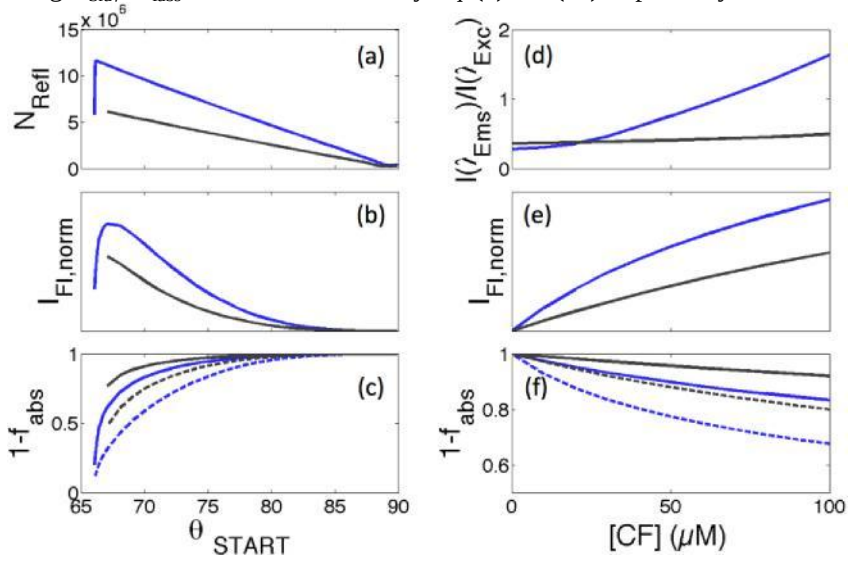

Fig. 7. Breakdown of calculated components for bent dcPCF (in blue) and scPCF (in grey) at ψ=0° with respect to (a,b,c) θ_{START} and (d,e,f) CF concentration. Solid and dotted lines for 1-f_{abs} plots correspond to that at λ_{ems} and λ_{exc}.

Additionally, a smaller a would essentially imply more frequent reflections and therefore a larger $N_{Refl.}$ This effectively dominates in $I_{Fl,norm}$ (Eq. **(11)** and **(12)**) and $_{1-fabs}$ (Eq. **(14)** and **(15)**), both scaling to the power of $N_{Refl.}$ Specifically, the former is large while the latter is

small at smaller $_{\theta START}$ values, as shown in Fig. 7a. Note that the jump in $_{NRefl}$ ^{at} $_{\theta START}$ values close to $_{\theta Crit}$ was a result of launched rays being refracted; hence $_{NRefl}$ is 0 for such rays. On the other hand, although CF concentrations linearly scale $_{Sray}$ ^{and} $_{fabs}$ values, the eventual calculations of $_{IFl,norm}$ ^{and} $_{1-fabs}$ were still dominated by $_{NRefl.}$ Lastly, the difference between the $_{1-fabs}$ plots for λ_{ems} $(1-f_{abs,ems})$ ^{and} λ_{exc} $(1-f_{abs,exc})$ was due to a larger ε for the latter, which hence led to lesser remaining excitation. With reference to Eq. **(5)**, a more rapidly decreasing $1-f_{abs,exc}$ with increasing CF concentrations and the inherently smaller $_{IFl,norm(\lambda exc),}$ causes $I(\lambda_{ems})/I(\lambda_{exc})$ to increase in the observed exponential manner.

Next in Fig. 6b, the scPCF plots for the bent configuration, were observed to only be agreeable upon adjustment of its $_{\theta START}$ span. This involved shortening the span and commencing it from 67.1˚, instead of the original 66.1˚ $_{(\theta Crit).}$ Interestingly, back calculating n_m using 67.1˚ as $_{\theta Crit,}$ gave a larger refractive index of 1.3474. This larger n_m could however be understood as the effective refractive index of the dye-filled air holes surrounding the core, which upon further inspection of the scPCF's cross section does concur with the more significant presence of the fused silica material between said air holes.

Contrasting between the bent PCFs, highlights two advantages of dcPCFs: (1) higher sensitivity and (2) higher repeatability, particularly at lower CF concentrations. These could primarily be attributed to its much larger $_{NRefl}$ values, which as shown in Fig. 7 and discussed earlier results in larger $_{IFl,norm}$ and smaller $_{1-fabs}$ values. Furthermore, the lower repeatability experienced in the scPCF experiments, were also deduced to be a result of its lower radial homogeneity due to the earlier mentioned significance of fused silica. This implied that upon bending, the x'-axis had a much higher probability of crossing a fused silica segment (between two air holes), instead of a dye-filled air hole. For the same reason, it extends to explain why the ray-tracing model produced a less coherent fit for the scPCF. Nonetheless, the difference between the bent and straight configurations was still identical for both PCFs.

Notably, the above discussed calculations only required the experimental inputs of a corresponding reference spectrum, $_{I0(\lambda)/I0(\lambda exc),}$ and figures describing CF's optical properties – ε, $_{fFl}$ ^{and} Φ_{Fl}.

4. Conclusion

A ray-tracing model was demonstrated to be effective in the computation of in-fiber light-matter interactions in index guiding PCFs – a dcPCF and a scPCF. This was attained via the simplification of said PCFs' core into cylinders, and plotting the trajectory of rays propagating via TIR along its length. The light-matter (light-fluorescence) interactions experienced at each point of reflection were further accounted for through calculations of absorption and collectable fluorescence emission. Subsequently, these interactions were summed over their total number of occurrences and averaged over all the launched rays. Combining these components produced the dimensionless ratio, $_{I(\lambda ems)/I(\lambda exc),}$ which served in the experiment to not only mitigate the effects of intensity fluctuations but also to exclude the need for optical filters. Comparing the experimental and calculated values validated the described model – particularly for the dcPCF. However, this was also limited by the accuracy of the earlier made cylindrical approximations, as shown by the observed discrepancies for the scPCF whose core possessed a less continuous perimeter of medium.

Appendix

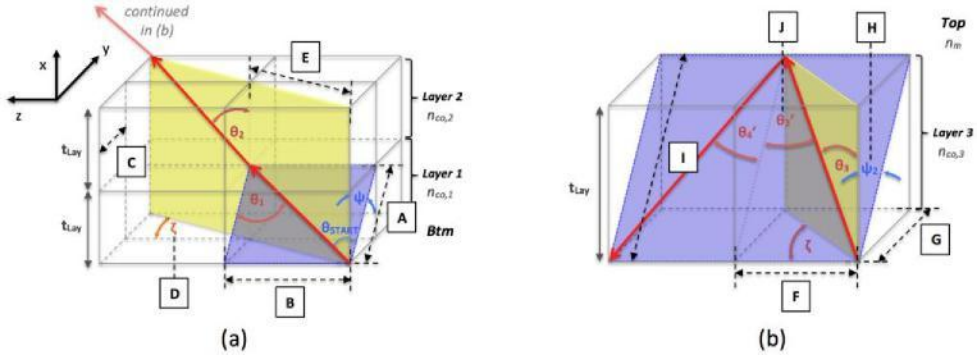

Fig. 8. Alternate view (90˚ counter-clockwise rotation about x-axis) of Fig. 4. Path of ray (in red) undergoing (a) refraction and (b) reflection in a 3D-domain, launched at a tilt of ψ. Plane of launch (for (a)) or incidence (for (b)) and Plane of refraction is highlighted in blue and yellow, correspondingly.

æ ö

The following lists the derivation for the symbols indicated in Fig. 4 and Fig. 8, for the

è *Lay* ø

refraction (A to E) and reflection (F to J) regime.

(17)

(18)

(19)

(20)

(21)

(22)

(23)

(24)

(25)

(26)

On the other hand, the following accounts for the different ranges of a described in Eq. **(9)**, where 1: $0 \le a \le a_{crit}$, 2: $a_{crit} \le a \le \pi/2$ and 3: $\pi/2 \le a \le \pi$.

(27)

(28)

(29)

Where the Fresnel coefficients are and ,

while *const* is a constant that can be ignored in Eq. **(9)**.

Acknowledgment

This work is supported by the Agency for Science Technology and Research through the Advanced Optics in Engineering Programme and Graduate Scholarship. We would also like to thank Yangtze Optical Fibre and Cable Company Ltd. (YOFC) for assisting with the fabrication of the PCF.